UCRL-ID-139407

Calculation of ^{239}Pu(n,n') Cross Sections to 5 MeV

H. Chen, M. A. Ross, G. Reffo, R. M. White

April 1, 2000

U.S. Department of Energy

Lawrence
Livermore
National
Laboratory

DISCLAIMER

This work was performed under the auspices of the U. S. Department of Energy by the University of California, Lawrence Livermore National Laboratory under Contract No. W-7405-Eng-48.

Calculation of $^{239}\mathrm{Pu}(n, n')$ Cross Sections to 5 MeV

H. Chen, M.A. Ross, G. Reffo, R.M. White

April 2000

Lawrence Livermore National Laboratory

Abstract

Calculations of the $^{239}\mathrm{Pu}(n, n')$ cross section and other relevant cross sections for incident neutron energies of up to 5 MeV are presented. Two components of the $^{239}\mathrm{Pu}(n, n')$ cross section are included. The direct contribution to the $^{239}\mathrm{Pu}(n, n')$ cross section is computed by the coupled-channel optical model. The compound component is calculated by a Hauser-Feshbach statistical treatment. Fission and γ-cascade processes are considered as competing channels in the compound-decay process. Whenever possible, calculations are compared with experimental data and evaluations.

1 Introduction

The neutron inelastic scattering cross section on isotopes contained in a system greatly affects the neutron flux[1]. Modeling the $^{239}\mathrm{Pu}(n, n')$ cross section is important because of the difficulty of measuring this cross section. The inelastic scattering cross section to the low-lying discrete states of $^{239}\mathrm{Pu}$ was not as complete in the ENDL-legacy library as it could be made with current modeling techniques. This report presents a recent calculation of the $^{239}\mathrm{Pu}(n, n')$ cross section for incident neutron energies up to 5 MeV. Nineteen discrete levels of $^{239}\mathrm{Pu}$ are included in the calculations. The inelastic cross section to all these levels as well as to the continuum are computed. Contributions to the $^{239}\mathrm{Pu}(n, n')$ cross section from direct and compound reaction mechanisms are taken into account. Fission and γ-cascade processes are included as competing channels in the compound component of the cross section calculations. The preequilibrium emission of neutrons is small when the incident neutron energy is less than 5 MeV and it is not included in this calculation.

2 Results and Discussions

The total cross section, $\sigma_{\mathrm{n,t}}$, is related to the reaction cross section, $\sigma_{\mathrm{n,R}}$, and the shape elastic scattering cross section, $\sigma_{\mathrm{n,se}}$, by

$$\sigma_{\mathrm{n,t}} = \sigma_{\mathrm{n,R}} + \sigma_{\mathrm{n,se}} \,. \tag{1}$$

The total elastic scattering cross section, denoted by $\sigma_{\mathrm{n,el}}$, is the sum of the shape elastic scattering cross section and compound elastic scattering cross section, $\sigma_{\mathrm{n,ce}}$:

$$\sigma_{\mathrm{n,el}} = \sigma_{\mathrm{n,se}} + \sigma_{\mathrm{n,ce}} \,. \tag{2}$$

In the energy range below 5 MeV, the reaction cross section consists of four components: the fission cross section, the inelastic scattering cross section, the compound elastic scattering cross section, and the capture cross section. They are denoted by $\sigma_{\mathrm{n,f}}$, $\sigma_{\mathrm{n,n'}}$, $\sigma_{\mathrm{n,ce}}$, and $\sigma_{n,\gamma}$, respectively. Thus,

$$\sigma_{\mathrm{n,R}} = \sigma_{\mathrm{n,f}} + \sigma_{\mathrm{n,n'}} + \sigma_{\mathrm{n,ce}} + \sigma_{\mathrm{n},\gamma} \,. \tag{3}$$

In the absence of preequilibrium emission, the inelastic scattering cross section $\sigma_{\mathrm{n,n'}}$ is composed of direct and compound components. The total cross section, reaction cross section, shape elastic scattering cross section, and the direct component of the inelastic scattering cross section, are obtained from the optical model which describes the mechanism of direct reactions[2]. The statistical model of Hauser-Feshbach[3] describes the mechanism of compound reactions which in this case include neutron emission, fission and capture. The transmission coefficients for particle emission are obtained from the optical model calculations. The fission transmission coefficients are calculated from the double-humped fission barrier model of Bjornholm and Lynn[4]. The transmission coefficients for γ-emission are derived from the γ-ray strength function whose shape, as a function of the γ-ray energy, is modeled by a Lorentzian[5]. We used the ECIS code[6] for optical model calculations and the IDA system of codes[5] for the calculation of the compound elastic scattering cross section, the compound component of the inelastic scattering cross section, the fission cross section, and the capture cross section.

2.1 Total Cross Section

The ground state of the ^{239}Pu nucleus is deformed. Therefore, the coupled-channel[7, 8] option in ECIS is used. Specifically, the first five discrete states of the ground state band of the ^{239}Pu are coupled. Their excitation energy (in keV), spin, and parity are, respectively, $(0.0,\frac{1}{2}^+)$, $(7.9,\frac{3}{2}^+)$, $(57.3,\frac{5}{2}^+)$, $(75.7,\frac{7}{2}^+)$ and $(163.8,\frac{9}{2}^+)$. Optical model parameters by Dietrich for the actinides[9] are first used as a starting point for the optical model calculations. Then the optical model parameter fitting routine BIGLAZY is used[5, 10] to fit the parameters to the experimental total cross section as well as data on the elastic scattering angular distributions. Due to energy resolution of the measurements, the experimental elastic angular distribution data also contain inelastic scattering cross sections. Consequently, the calculated inelastic scattering cross section to the first four excited states are added to the calculated elastic cross

section in the fitting procedure. The IDA system of nuclear reaction codes is used to calculate the compound component of the inelastic scattering cross section to all nineteen discrete states. As a result, a coupling between the codes ECIS and IDA is made. The best fit to the total cross section was determined when the ground state quadrupole and hexadecupole deformation parameters for ^{239}Pu are $\beta_2 = 0.2$ and $\beta_4 = 0.06$, respectively. Figure 1 shows the resultant total cross section. The ENDL99 curve in Figure 1 is the latest evaluation of LLNL with an estimated uncertainty of 1% above 300 keV[11]. It is to this evaluation that the calculated total cross section is fitted. As can be seen from Figure 1, the fitted parameters for the optical potential with the static deformation of the ^{239}Pu nucleus give a good fit to the ENDL99 evaluation.

2.2 Reaction Cross Section

The split of the total cross section into reaction and shape elastic scattering cross section is determined by the optical model. Limited experimental data on the total elastic scattering cross section and elastic angular distributions make quantifying the uncertainty of the calculated reaction cross section difficult. To further complicate the matter, the total elastic scattering cross section has a compound component which is non-negligible at the incident neutron energies considered here. Experimentally, elastically scattered neutrons from direct and compound processes are indistinguishable. Theoretically, the two processes are described by different models, each of which has its own set of parameters. We calculated the reaction cross section with the optical model parameters derived from the aforementioned BIGLAZY fit. In order to compare with the available experimental data, the total elastic scattering cross section, $\sigma_{\mathrm{n,el}}$, and the nonelastic scattering cross section, $\sigma_{\mathrm{n,nonel}}$, are calculated and shown in Figures 2 and 3, respectively. These cross sections are defined by

$$\sigma_{\mathrm{n,t}} = \sigma_{\mathrm{n,el}} + \sigma_{\mathrm{n,nonel}} \quad (4)$$

$$\sigma_{\mathrm{n,R}} = \sigma_{\mathrm{n,nonel}} + \sigma_{\mathrm{n,ce}} \, . \quad (5)$$

The corresponding evaluations from ENDL-legacy, ENDF/B-VI[12], JENDL[13] and JEF[14] are also shown in Figures 2 and 3. The experimental data on the $\sigma_{\mathrm{n,el}}$ cross section in Figure 2 are found from the EXFOR[15] data base. Again, energy resolutions of the experiments were such that inelastic scattering cross sections to the low-lying states are included in these data[16, 17]. Two sets of ECIS-IDA calculations are presented in both figures. One corresponds to fission cross section calculations using parameters adjusted by the automatic fitting program STEW[18]. The other is the same calculation based on Bjornholm and Lynn's fission parameters. The difference between these two curves is due to the different compound elastic scattering cross sections which are influenced by the choice of fission parameters. One sees from Figure 2 that the guidance from experimental data on even the total elastic scattering cross section is limited. While most evaluations are reasonably similar, the two sets

of ECIS-IDA calculations agree better with the ENDF/B-VI and JENDL evaluation for incident neutron energy $E_{inc} > 1$ MeV. Shown in the lower portion of Figure 2 are compound components of the elastic scattering cross section calculated by ECIS-IDA. Clearly seen is that although $\sigma_{\mathrm{n,ce}}$ is small in comparison to $\sigma_{\mathrm{n,el}}$, it is not negligible in this incident neutron energy range.

Figure 3 shows some experimental data of the ^{239}Pu(n,nonel) cross section obtained from the EXFOR and the ECSIL[19] data bases. As in Figure 2, the ENDL-legacy, ENDF/B-VI, JENDL and JEF evaluations together with two sets of ECIS-IDA calculations are plotted. Because of the non-vanishing $\sigma_{\mathrm{n,ce}}$ cross section, neither $\sigma_{\mathrm{n,el}}$, nor $\sigma_{\mathrm{n,nonel}}$ gives a direct measure of the reaction cross section, $\sigma_{\mathrm{n,R}}$. Until further experimental data on the $\sigma_{\mathrm{n,el}}$ cross section becomes available (perhaps for higher incident neutron energies), one is limited to using optical model parameters that best reproduce the total cross section for which there are abundant experimental data, while using the experimental data on the $\sigma_{\mathrm{n,el}}$ and the $\sigma_{\mathrm{n,nonel}}$ cross sections as a crude guide for the theoretical calculation of the reaction cross section σ_{R}. For the rest of the report, optical model parameters obtained from the BIGLAZY fit are employed in our calculations.

2.3 Components of Reaction Cross Section

As mentioned in Section 1, there are four components of the reaction cross section considered in this paper. The largest is the fission cross section. Figure 4 displays the IDA calculation of $\sigma_{\mathrm{n,R}}$ and its four components. As the incident neutron energy increases, a decrease in the $\sigma_{\mathrm{n,ce}}$ cross section and an increase in the $\sigma_{\mathrm{n,n'}}$ cross section is observed. This is easily understood as the number of inelastic channels that are open at higher incident neutron energies is large in comparison to the single elastic channel. Similarly, the increasing probability of particle emission causes the capture cross section to decrease steadily with E_{inc} and it practically vanishes when $E_{inc} > 3$ MeV.

Since fission is the major component of the reaction cross section, the accuracy of its calculation is important in determining the magnitudes of the other reaction channels. The existence of reliable experimental data on fission cross section makes it possible to adjust the parameters used in the fission model such that the calculated fission cross section agrees well with that evaluated from experiments. An automatic non-linear parameter search program, STEW, based on the Levenberg-Marquardt algorithm[20] was written to carry out the parameter adjustment. Figure 5 shows the significant improvement of the fission cross section calculated with parameters derived from STEW over that calculated with default parameters from Bjornholm and Lynn. Note that the determination of these fission parameters is dependent on the choice of the parameters in the optical model. STEW fitted the fission parameters to the lastest fission cross section evaluation labeled as ENDL99 in the figure. The uncertainty associated with this evaluation is less than 2%[11]. In the fitting process,

the two fission barrier heights and curvatures at the two saddle points, the nuclear temperature, and the multiplicative factor in the constant temperature level density formula used for the calculation of fission transmission coefficient, were adjusted. Also shown in Figure 5 are the evaluations of fission cross section from ENDF/B-VI, JENDL and JEF. It should be stressed that the agreement between the calculated and the evaluated fission cross sections does not eliminate the uncertainty associated with the the calculation of the reaction cross section. It simply excludes fission as a source of error in the calculated total inelastic scattering cross sections.

The calculated capture cross section is shown in Figure 6 together with some experimental data found in the ECSIL data base as well as other major evaluations. The other two components of the reaction cross section are the compound elastic scattering cross section and the inelastic scattering cross section. Results of the compound elastic scattering cross section are shown in Figure 2 and the inelastic scattering cross section will be discussed in the next section.

2.4 Inelastic Scattering Cross Section

The main focus of this report is the inelastic scattering cross section, $^{239}\mathrm{Pu}(n,n')$. Figure 7 shows the two calculations from IDA of the total $^{239}\mathrm{Pu}(n,n')$ cross section as well as evaluations and the limited experimental data available. One IDA calculation is carried out with fission parameters obtained from STEW, the other with fission parameters from Bjornholm and Lynn. The large difference between the calculated fission cross sections from the two sets of fission parameters (c.f. Figure 5) is seen to greatly affect the magnitude of the total inelastic cross section, particularly between 1 and 5 MeV. The apparently lower $^{239}\mathrm{Pu}(n,n')$ cross section from threshold to about $E_{\mathrm{inc}} = 0.025$ MeV from our calculations is largely due to the higher fission cross section from our calculations in this energy range (c.f. Figure 5).

Inelastic scattering comes from both direct and compound processes in the range of incident neutron energy considered in this report. The direct inelastic scattering cross section component to the first four discrete excited states of $^{239}\mathrm{Pu}$ are calculated since those are the "coupled-channels". The compound inelastic scattering to both discrete and continuous portions of the the excitation spectrum of $^{239}\mathrm{Pu}$ are considered. A breakdown of the total $^{239}\mathrm{Pu}(n,n')$ cross section into various components is given in Figure 8 where

$$\sigma_{\mathrm{n,n'}} = \sigma_{\mathrm{n,n'}}^{\mathrm{direct}} + \sigma_{\mathrm{n,n'}}^{\mathrm{compound}} \tag{6}$$

$$\sigma_{\mathrm{n,n'}}^{\mathrm{compound}} = \sigma_{\mathrm{n,n'}}^{\mathrm{compound-discrete}} + \sigma_{\mathrm{n,n'}}^{\mathrm{compound-continuous}} . \tag{7}$$

The $\sigma_{\mathrm{n,n'}}^{\mathrm{compound-discrete}}$ cross section is calculated for each of the first 19 excited states of $^{239}\mathrm{Pu}$ given in Table 1. Uncertainties in either angular momentum or parity assignments for the discrete levels as well as missing levels from experiments occur at higher

excitation energies. Consequently, the continuous Gilbert-Cameron[21] level density formula is used beyond the nineteenth excited state. Figure 8 shows, as expected, that the $\sigma_{n,n'}^{\text{compound-discrete}}$ cross section first increases with E_{inc} as more discrete (n,n') channels open up. When E_{inc} is high enough such that the $\sigma_{n,n'}^{\text{compound-continuous}}$ channel is open, one sees a decrease in $\sigma_{n,n'}^{\text{compound-discrete}}$ and at the same time, an increase in $\sigma_{n,n'}^{\text{compound-continuous}}$. The $\sigma_{n,n'}^{\text{direct}}$ cross section, on the other hand, is decoupled from the compound process and mostly follows the behavior of the total cross section which has a rise between 3 and 4 MeV (see Figure 1). The small (n,gx) cross section describes the process where a photon is emitted first, followed by the emission of a particle which is a neutron in this energy range. The (n,gx) cross section is therefore considered as a component of the total inelastic scattering cross section.

Figure 9 shows the compound-continuous component of the inelastic scattering cross section from our current calculation and several evaluations. One sees that the difference between various evaluations is large and our calculation comes slightly under all evaluations for $E_{\text{inc}} < 2$ MeV. On the other hand, in the range of $2 < E_{\text{inc}} < 5$ MeV, our calculation is higher than all the evaluations except ENDL-legacy. The value of E_{inc} at which the compound-continuous component of the inelastic scattering starts depends, of course, on the number of discrete levels included in the calculations. For example, ENDF/B-VI employs the first 31 discrete levels versus 19 that are used in our calculation. On the other hand, ENDL-legacy had only 6 discrete levels included in the evaluation. One therefore sees that the ENDL-legacy curve in Figure 9 starts at a lower E_{inc} than our current calculation which in turn starts at a lower E_{inc} than the ENDF/B-VI evaluation. The magnitude of the $\sigma_{\text{n,n'}}^{\text{compound-continuous}}$ cross section at a given incident neutron energy, E_{inc}, is determined by several factors in addition to where the discrete states terminate. The first is the magnitude of the reaction cross section which depends on the optical model potential used. Secondly, the size of the direct inelastic scattering cross section, which is also derived from the details of the optical model calculation, determines the magnitude of the compound component of the reaction cross section. The compound reaction cross section subsequently is a sum of the compound elastic scattering cross section, the capture cross section, the fission cross section and the compound inelastic cross section. Although the transmission coefficients for neutron emission are obtained from the optical model, the governing factor in the calculation of particle emission cross sections is probably the level density employed for the continuous energy spectrum. Calculations of the γ-emission transmission coefficient and the fission transmission coefficient depend on the models used to describe these processes and the choices of parameters embedded in the models. Level density also plays an important role in the calculation of the capture cross section although this cross section is small in comparison to others. The difference in the magnitude of the $\sigma_{\text{n,n'}}^{\text{compound-continuous}}$ cross section between our calculation and various evaluations seen in Figure 9 is a result of the convoluted interplay of all the above factors.

Figure 10 displays our calculated direct and compound inelastic scattering cross

sections to the first four excited states of ^{239}Pu. The four curves on the left-hand-side of the figure are the compound inelastic scattering cross sections and the four curves on the right-hand-side give the direct inelastic scattering cross sections. A few features are immediately apparent. First, all the excitation functions for the direct process peak at the same incident neutron energy that pretty much coincides with the local maximum of the total cross section, as expected. On the other hand, the peaks of the excitation functions for the compound process shift to the right as the excitation energy of the discrete state increases. This is because the higher the excitation energy of the discrete state, the higher the incident neutron energy required to maximize the probability of leaving the residual nucleus, after emission of a neutron, in that discrete state. Eventually, all these excitation functions tail off because of the opening up of the compound-continuous component of the inelastic scattering cross section. Another noticeable characteristic is that for the first four discrete states, the peak value of the excitation functions for the compound process decreases when the excitation energy of the excited state increases whereas this is not the case with the direct process. The $\sigma_{\mathrm{n,n'}}^{\mathrm{compound-discrete}}$ cross section to a specific discrete state depends on the behavior of the transmission coefficients as a function of energy and angular momentum of both the compound and residual nuclei. What we are seeing in Figure 10 is the outcome of all these competing contributions to the $\sigma_{\mathrm{n,n'}}^{\mathrm{compound-discrete}}$ cross section.

Figures 11 to 16 give the excitation functions of the inelastic scattering cross section to the first six excited states of ^{239}Pu. Both direct and compound components of the inelastic scattering are present in the first four excitation functions whereas only the compound component appears in the others. ENDL-legacy, ENDF/B-VI, JENDL, and JEF evaluations are also shown for comparison. Excitation functions of some discrete states are missing in the ENDL-legacy evaluation since it was based on experimental data available at the time. Although the general trend between various evaluations agree with each other, variations in magnitude are large. The local maximum of the direct inelastic scattering cross section around $E_{\mathrm{inc}} = 3$ MeV is seen to influence the shapes of the first four excitation functions (figures 11 to 14). This effect is most pronounced in the $E_x = 57$ keV (figure 12) excitation function followed by the $E_x = 7.9$ keV excitation function (figure 11), consistent with the results shown in Figure 10. In Figure 15, there are large differences between ENDF/B-VI, JENDL, JEF and our calculations. The reason for the difference is not clear but may depend on how many coupled-channels were used in these evaluations. We also do not know the input parameters used in the calculations for these evaluations. The excitation function of the next discrete state, shown in Figure 16, does show convergent behavior amongst various evaluations and our calculation. Notice the peak value of the $E_x = 285$ keV excitation function is much higher than that of the $E_x = 193$ keV excitation function. This is because the spin of the $E_x = 193$ keV state is much higher than that of the $E_x = 285$ keV state. The limited angular momentum the incident neutron brings, in the energy range of interest, makes the population of

the $E_x = 193$ keV state difficult.

3 Conclusion

In order to examine the inelastic scattering cross section for ^{239}Pu in the energy range less than 5 MeV, various relevant cross sections are calculated. While the total cross section agrees well with the experimental data, the uncertainty of the reaction cross section is difficult to quantify, and is probably within the range of 5% to 10%. With fission cross section determined by experimental data, error in the reaction cross section is propagated to the compound elastic scattering, capture, and inelastic scattering cross sections. Below 1 MeV, the magnitude of the inelastic scattering cross section is strongly influenced by the magnitude of the compound elastic scattering and capture cross sections. For $E_{\rm inc} > 1$ MeV, both the compound elastic scattering and capture cross sections become very small so that the uncertainty in the reaction cross section is almost entirely propagated to the inelastic scattering cross section. Assuming the fission cross section in the evaluations is adjusted to experimental data, the differences in Figure 7 between various evaluations and our calculation are therefore probably a result of the different parameters used in the optical model potential. The precise breakdown of the inelastic scattering cross section into various components mostly depends on the details of the models used in calculating the direct and compound components of the inelastic scattering cross section. The general characteristics and the relative magnitudes of the different components of the inelastic scattering cross section according to our calculation are given in Figure 8. Further breakdown of the $\sigma_{\rm n,n'}^{\rm compound}$ cross section into $\sigma_{\rm n,n'}^{\rm compound-discrete}$ and $\sigma_{\rm n,n'}^{\rm compound-continuous}$ cross sections, together with various evaluations, are given in Figures 9 to 16. In general, the differences between various evaluations and our calculation are larger for the individual components of the ^{239}Pu(n,n') cross section than they are for the total ^{239}Pu(n,n') cross section. This is most likely a reflection of the differences in the detailed input parameters used in each evaluation to calculate the components of the ^{239}Pu(n,n') cross section. From Figures 7 to 16, it is clearly seen that our current calculation used in ENDL99 is a significant improvement over the previous ENDL-legacy evaluation. This reflects the advances in nuclear reaction theories used to model the cross sections as well as new and improved experimental data, for example, on nuclear structure.

4 Acknowledgements

Discussions with Marshall Blann and Frank Dietrich on the calculations presented in this report are greatfully acknowledged.

References

[1] A.F. Henry, *Nuclear-Reactor Analysis*, M.I.T. Press, Cambridge, Massachusetts, (1975).

[2] P.E. Hodgson, "The Optical Model of Elastic Scattering", Oxford University Press, (1963).

[3] W. Hauser and H. Feshbach, *Phys. Rev.* **87**, 366(1952).

[4] S.E. Bjornholm and J.E. Lynn, "The Double-Humped Fission Barrier", *Rev. Mod. Phys.*, **52**, 725(1980).

[5] G. Reffo and F. Fabbri, IDA system of codes, ENEA, Bologna, Italy.

[6] J. Raynal, code ECIS95, unpublished.

[7] G.R. Satchler, "Introduction to Nuclear Reactions", Second Edition, Oxford University Press, (1990).

[8] E. Gadioli and P.E. Hodgson, "Pre-Equilibrium Nuclear Reactions", Oxford University Press, (1992).

[9] F. Dietrich, private communication.

[10] M.A. Ross, H. Chen, E. Ormand, and R.M. White, "A New LLNL Evaluation of Neutron Induced Reactions on ^{239}Pu", report in preparation, Lawrence Livermore National Laboratory, (2000).

[11] R.M. White, private communication.

[12] P. Rose, "ENDF-201: ENDF/B Summary Documentation", Fourth Edition (ENDF/B-VI), Brookhaven National Laboratory report, BNL-NCS-**17541**, (1992).

[13] T. Nakagawa, et al., "Japanese Evaluated Nuclear Data Library", Version 3, Revision 2, *J. Nucle. Sci. Technol.*, **32**, 1259(1995).

[14] C. Nordborg, M. Salvatores, "Status of the JEF Evaluated Data Library", Nuclear Data for Science and Technology, edited by J.K. Dickens (American Nuclear Society, LaGrange, IL, 1994).

[15] V. McLane, "EXFOR System Manual: Nuclear Reaction Data Exchange Format", Report BNL-NCS-**63330**, National Nuclear Data Center, Brookhaven National Laboratory, (1996).

[16] R.C. Allen, R.B. Walton, R.B. Perkins, R.A. Olson, and R.F. Taschek, "Interaction of 0.5 and 1.0 MeV Neutrons with Some Heavy Elements", *Phys. Rev.*, **104**, 731(1956).

[17] G. Haouat, J. Lachkar, Ch. Lagrange, J. Jary, J. Sigaud, and Y. Patin, *Nucl. Sci. Eng.*, **81**, 491(1982).

[18] H. Chen, "STEW: A Nonlinear Data Modeling Computer Program", UCRL-ID-**138276**, Lawrence Livermore National Laboratory, (2000).

[19] M.H. MacGregor, D.E. Cullen, R.J. Howerton, and S.T. Perkins, "Integrated System for Production of Neutronics and Photonics Calculational Constants", Neutron-induced Interactions, Index of Experimental Data. UCRL-**50400**, Volume 3, Revision 2. Lawrence Livermore National Laboratory, (1976).

[20] W.H. Press, S.A. Teukolsky, W.T. Vetterling, and B.P. Flannery, "Numerical Recipes", Second Edition, Cambridge University Press, (1992).

[21] A. Gilbert and A.G.W. Cameron, *Can. J. Phys.*, **43**, 1446(1965).

This work was performed under the auspices of the U.S. Department of Energy by Lawrence Livermore National Laboratory under Contract No. W-7405-ENG-48.

level	E_x (MeV)	J	parity
1	0.008	3/2	+
2	0.057	5/2	+
3	0.076	7/2	+
4	0.164	9/2	+
5	0.193	11/2	+
6	0.285	5/2	+
7	0.318	13/2	+
8	0.330	7/2	+
9	0.358	15/2	+
10	0.387	9/2	+
11	0.392	7/2	-
12	0.434	9/2	-
13	0.462	11/2	+
14	0.470	1/2	-
15	0.487	11/2	-
16	0.492	3/2	-
17	0.506	5/2	-
18	0.512	7/2	+
19	0.519	17/2	+

Table 1: The excitation energy, spin, and parity of the first 19 discrete levels of the ^{239}Pu nucleus.

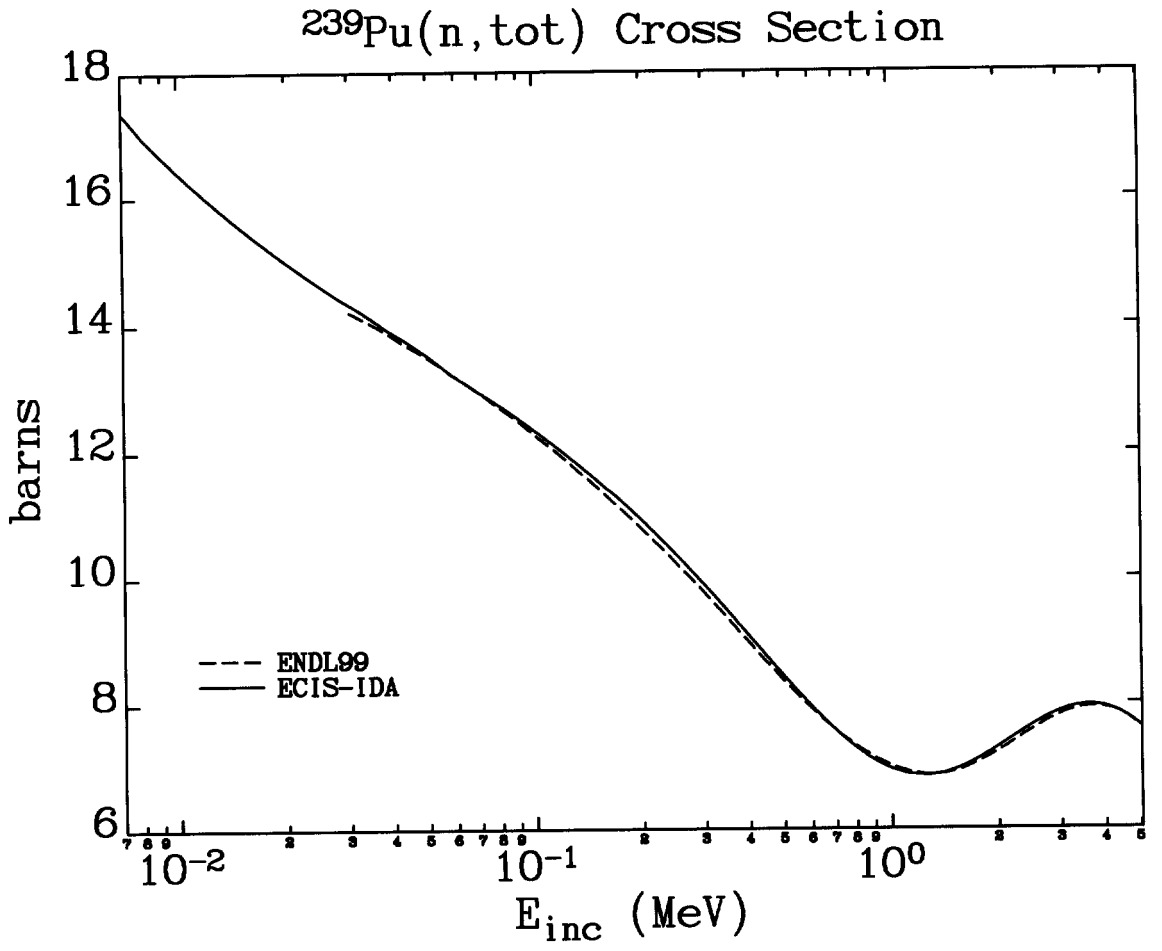

Figure 1: n+^{239}Pu *total cross section as a function of incident neutron energy.*

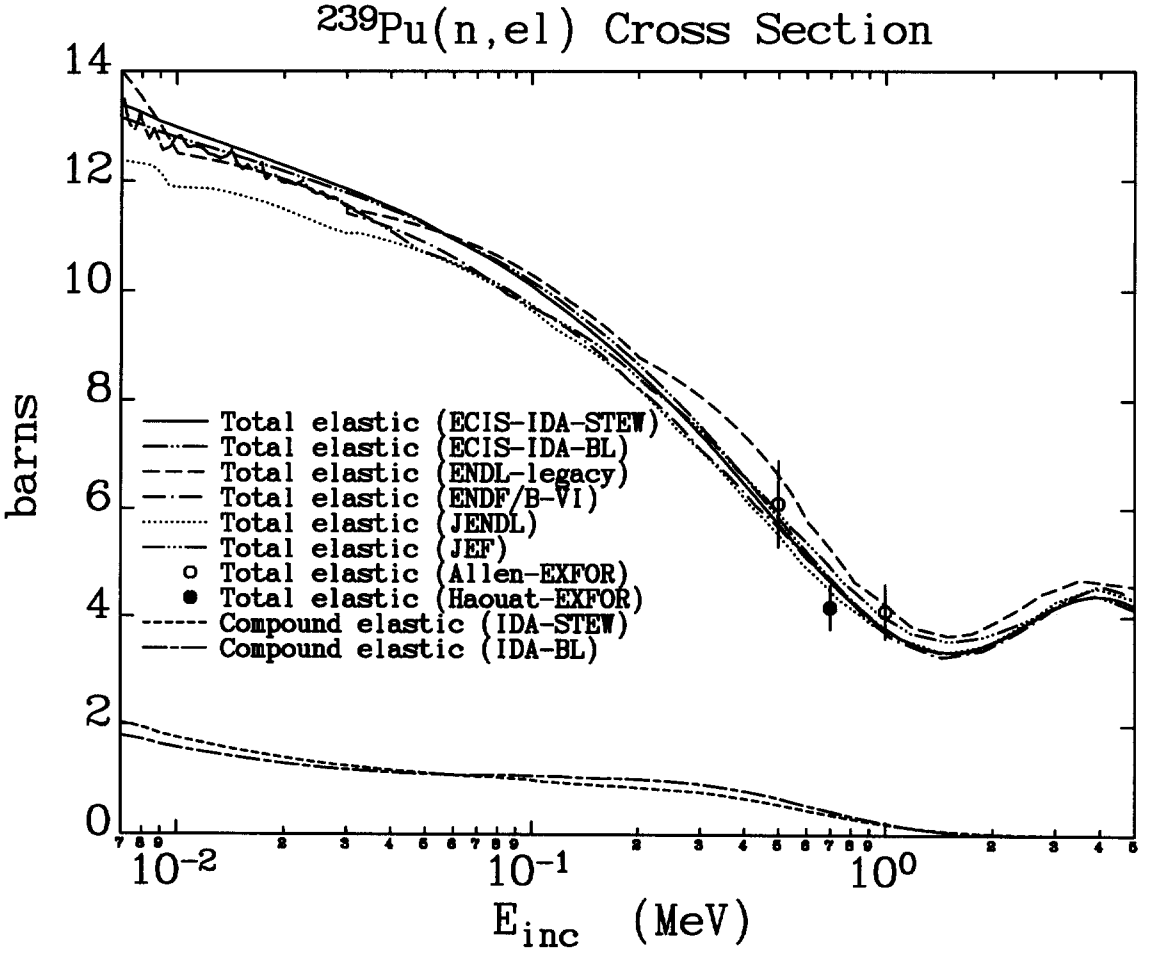

Figure 2: *Total elastic scattering cross section on ^{239}Pu as a function of incident neutron energy from two sets of ECIS-IDA calculations, several evaluations, and two sets of data. The two curves at the bottom of the plot are compound elastic scattering cross sections from the two sets of ECIS-IDA calculations.*

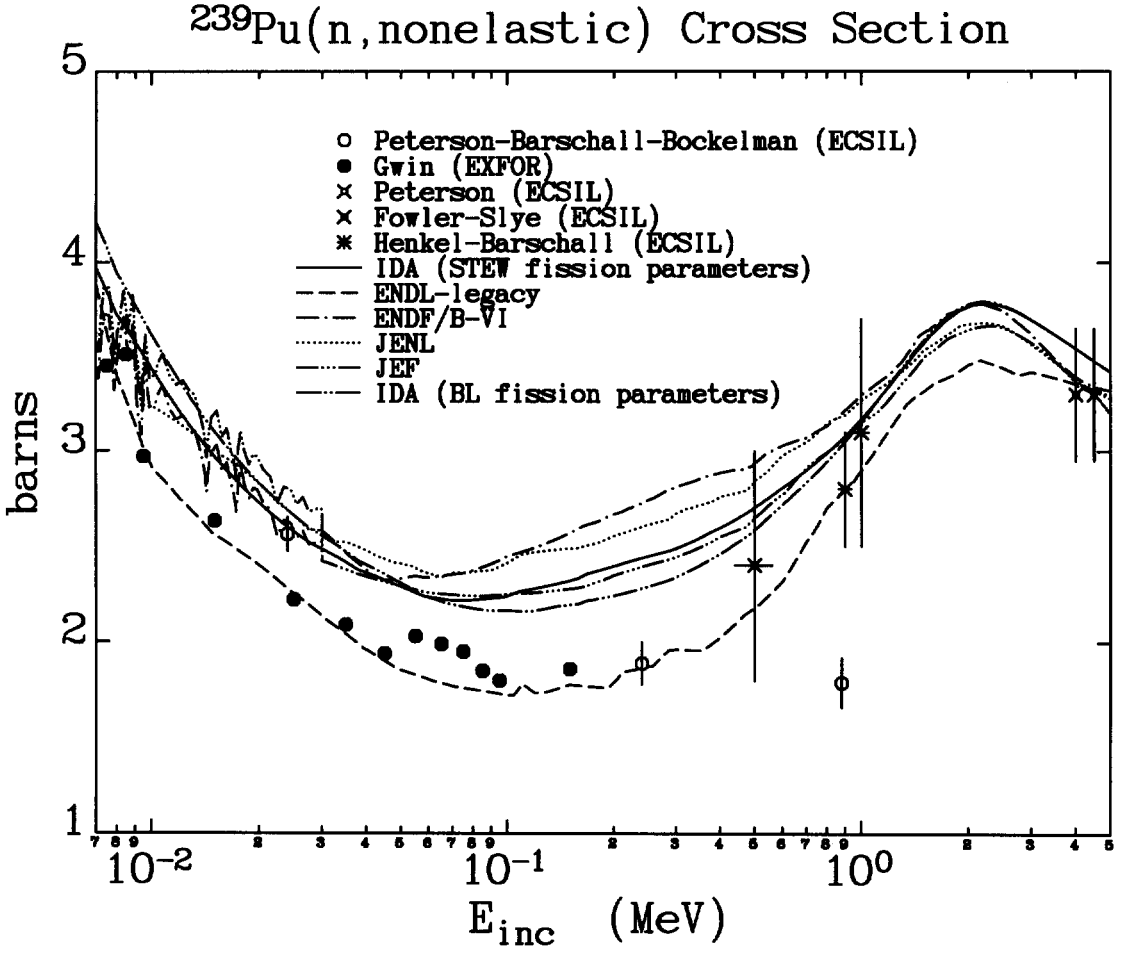

Figure 3: *Nonelastic scattering cross section on ^{239}Pu as a function of incident neutron energy from two sets of ECIS-IDA calculations, several evaluations, and five sets of data.*

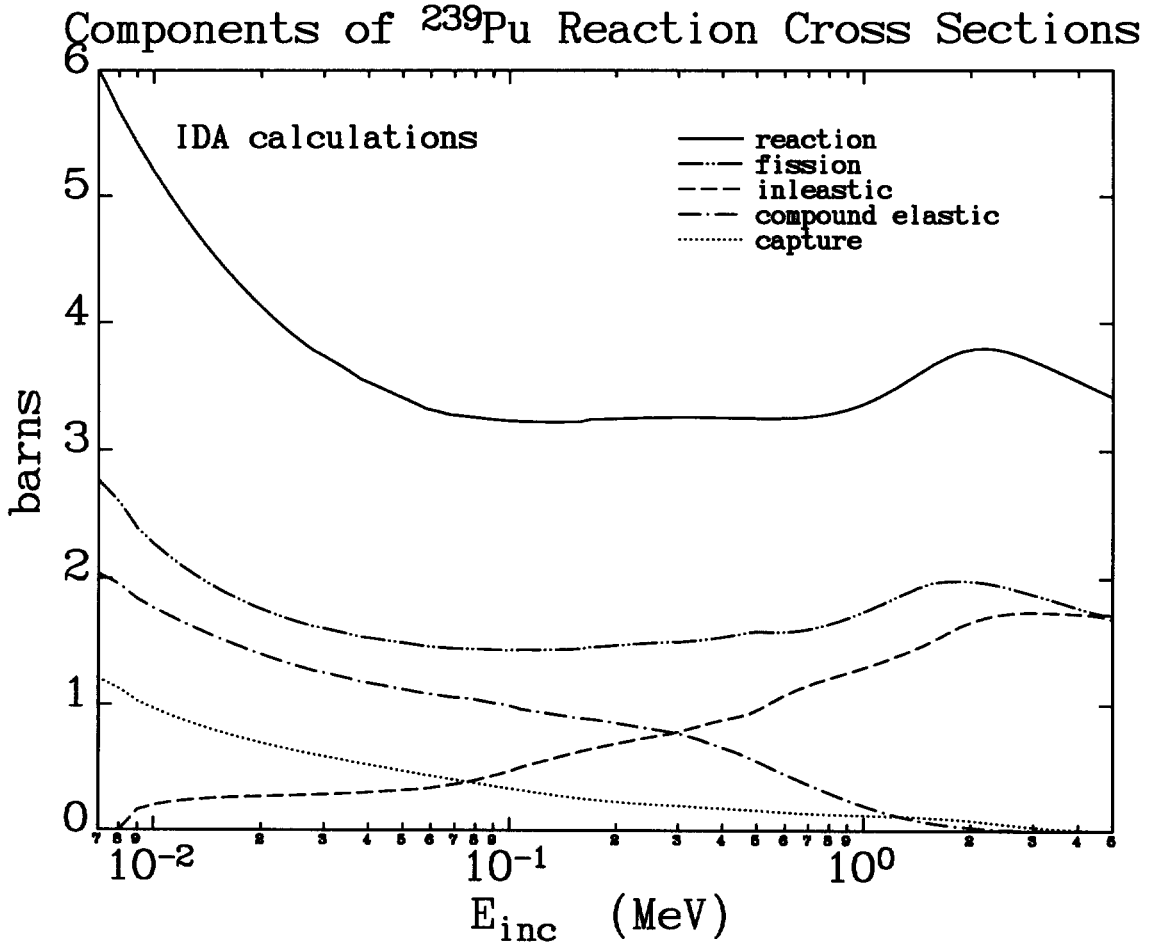

Figure 4: *n+^{239}Pu reaction cross section and its four components as a function of incident neutron energy.*

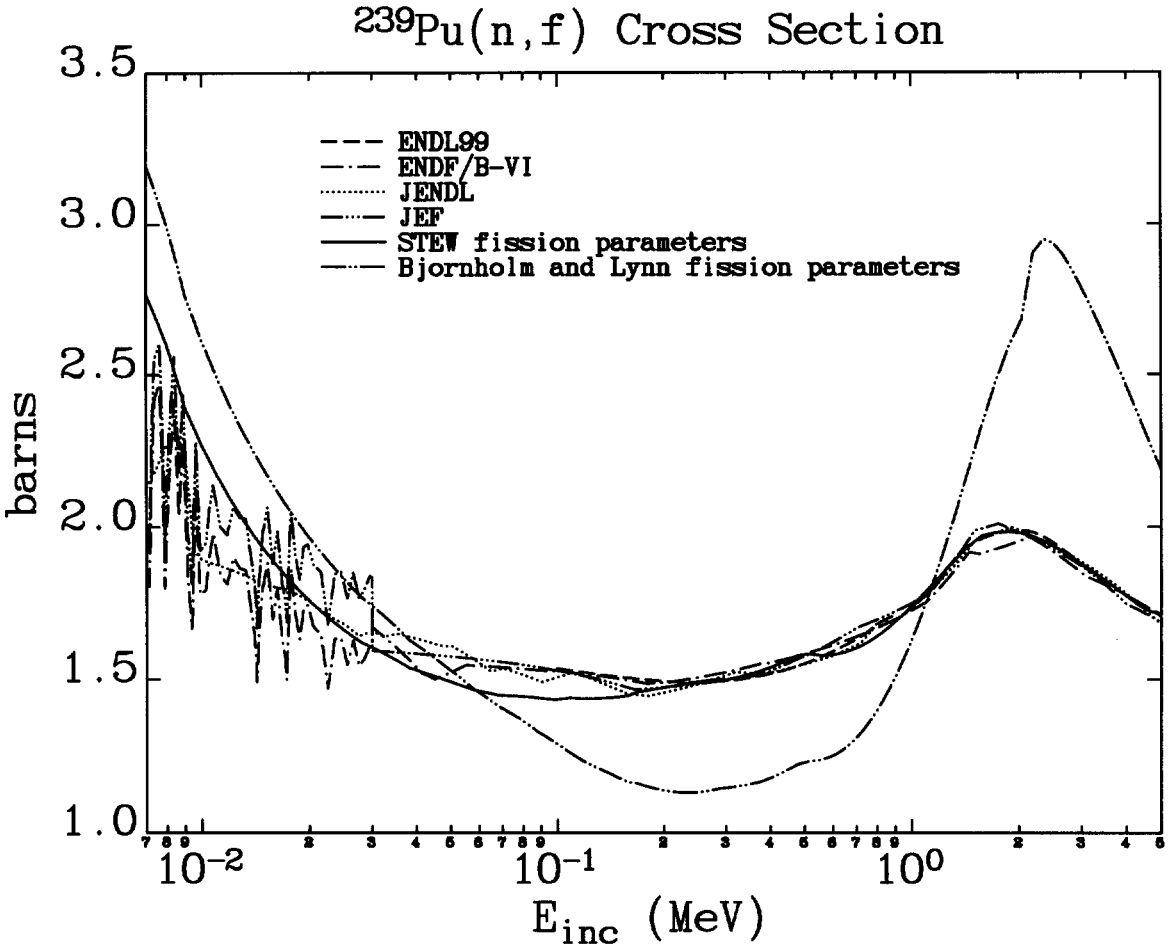

Figure 5: $^{239}Pu(n,f)$ *cross section as a function of incident neutron energy.*

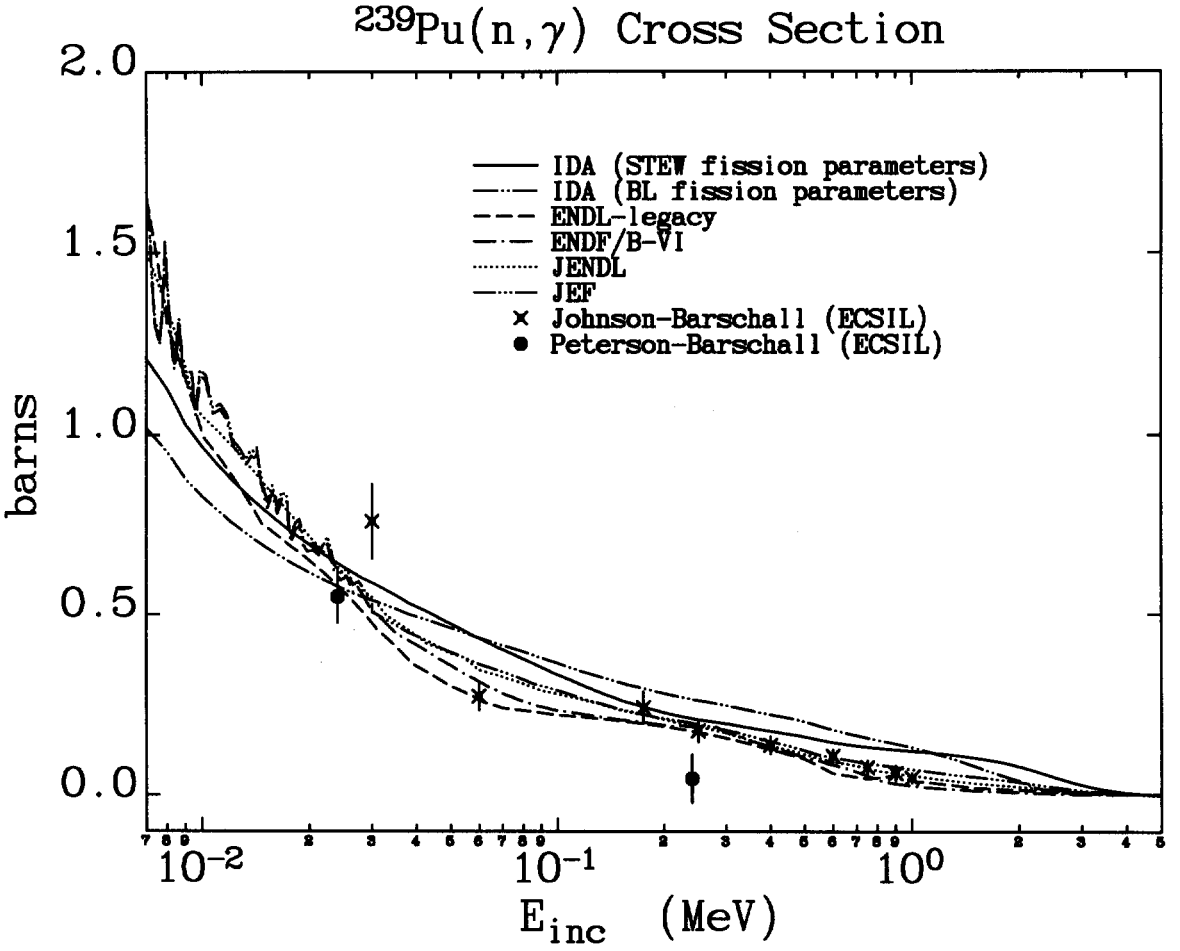

Figure 6: $^{239}Pu(n,\gamma)$ *cross section as a function of incident neutron energy.*

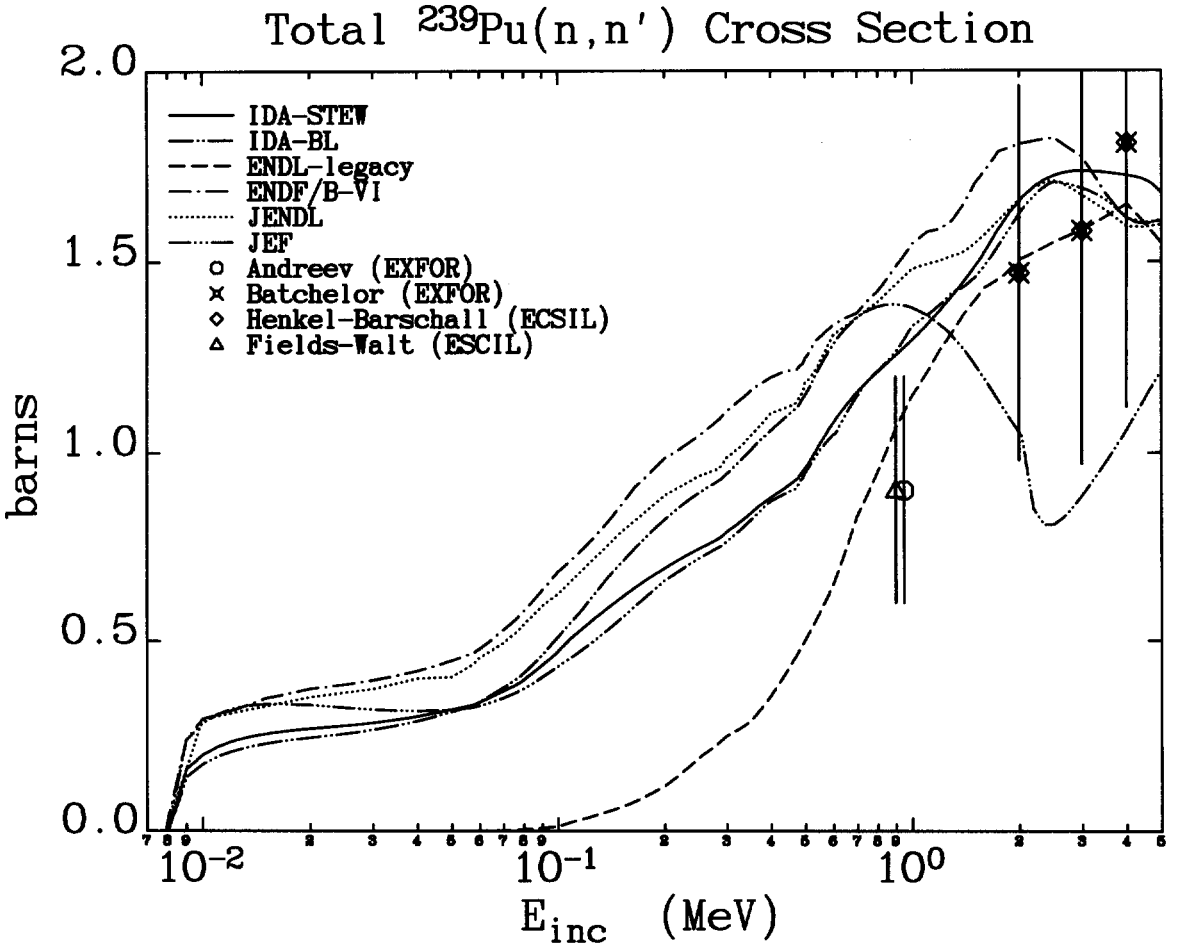

Figure 7: $^{239}Pu(n,n')$ *cross section as a function of incident neutron energy.*

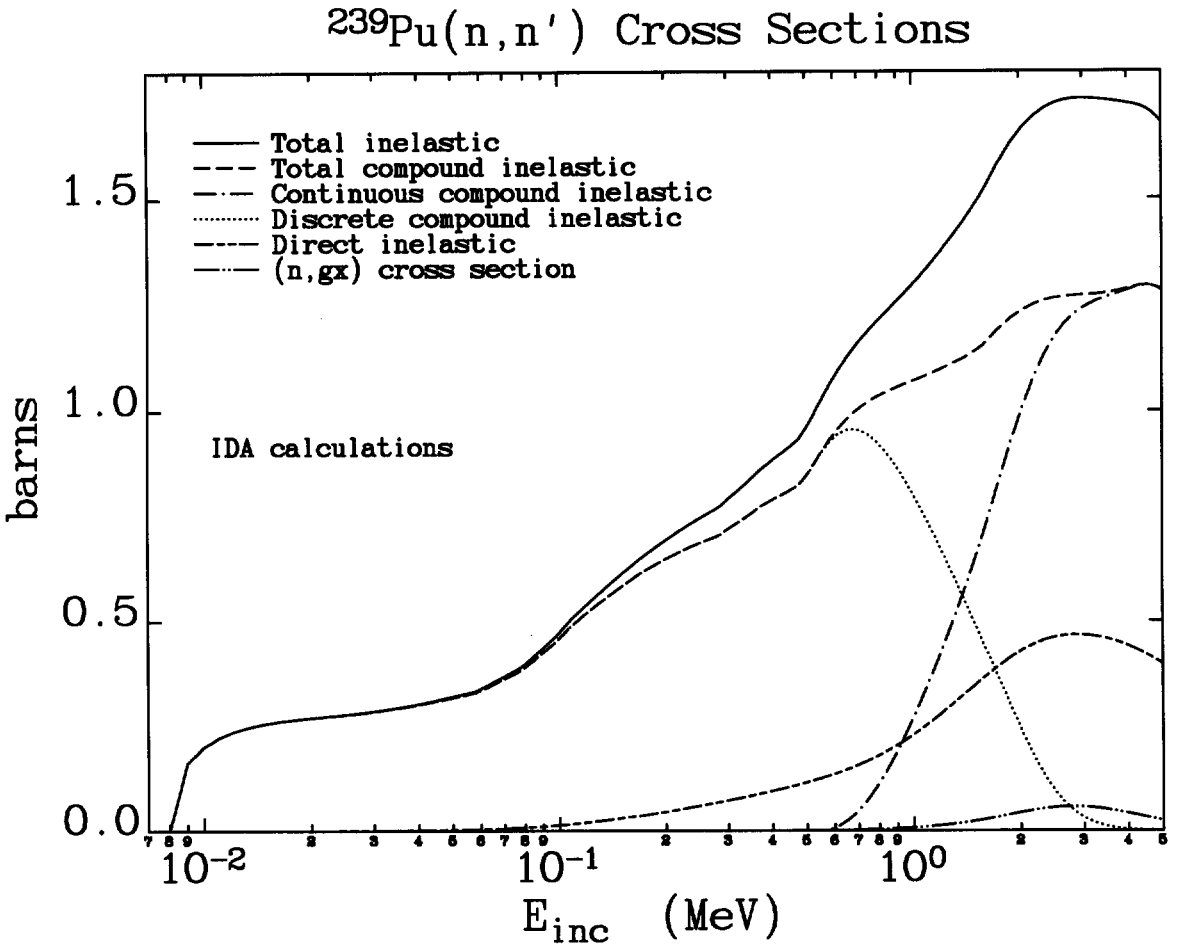

Figure 8: *A breakdown of the total* $^{239}Pu(n,n')$ *cross section as a function of incident neutron energy.*

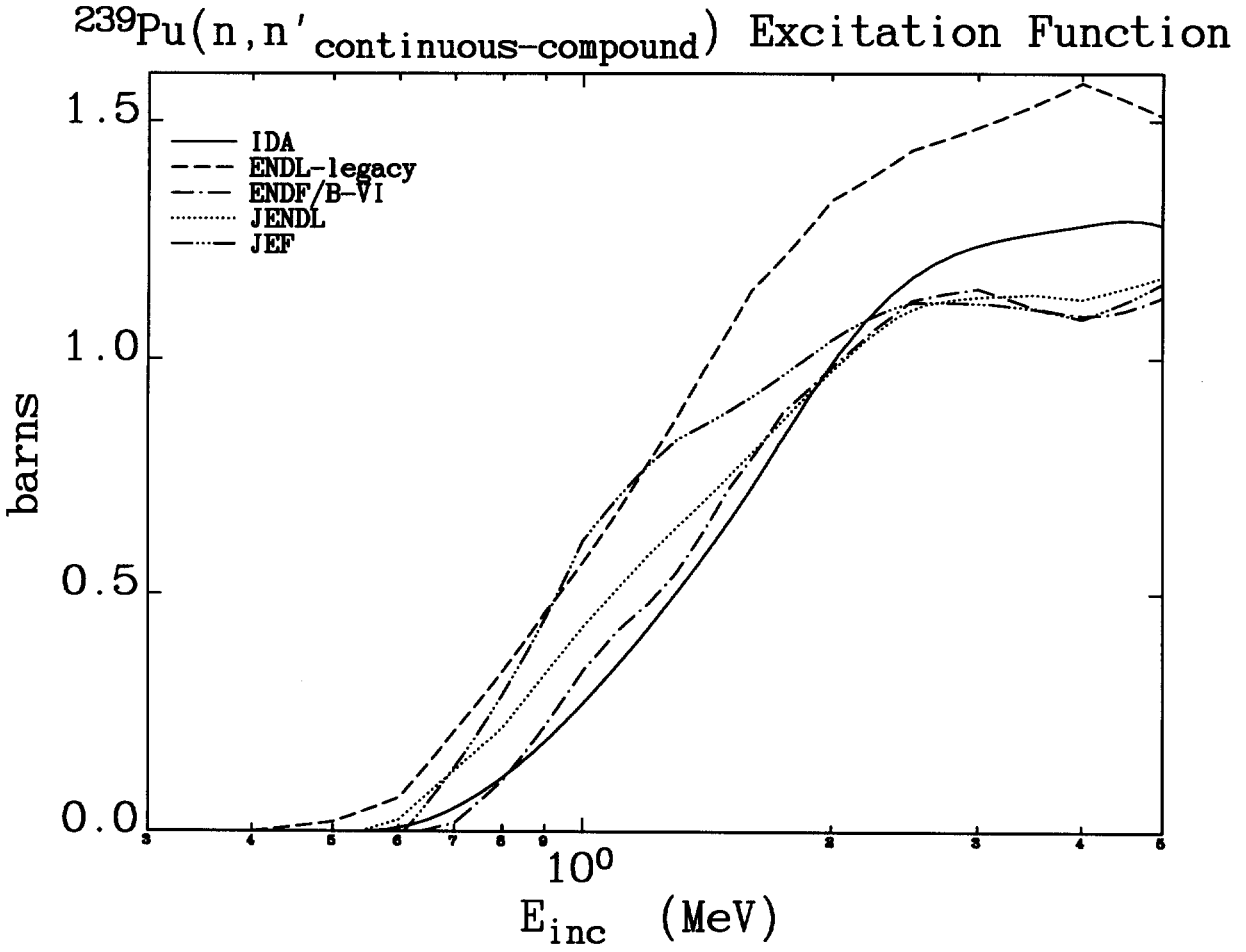

Figure 9: *The compound-continuous component of the* $^{239}Pu(n, n')$ *cross section as a function of incident neutron energy.*

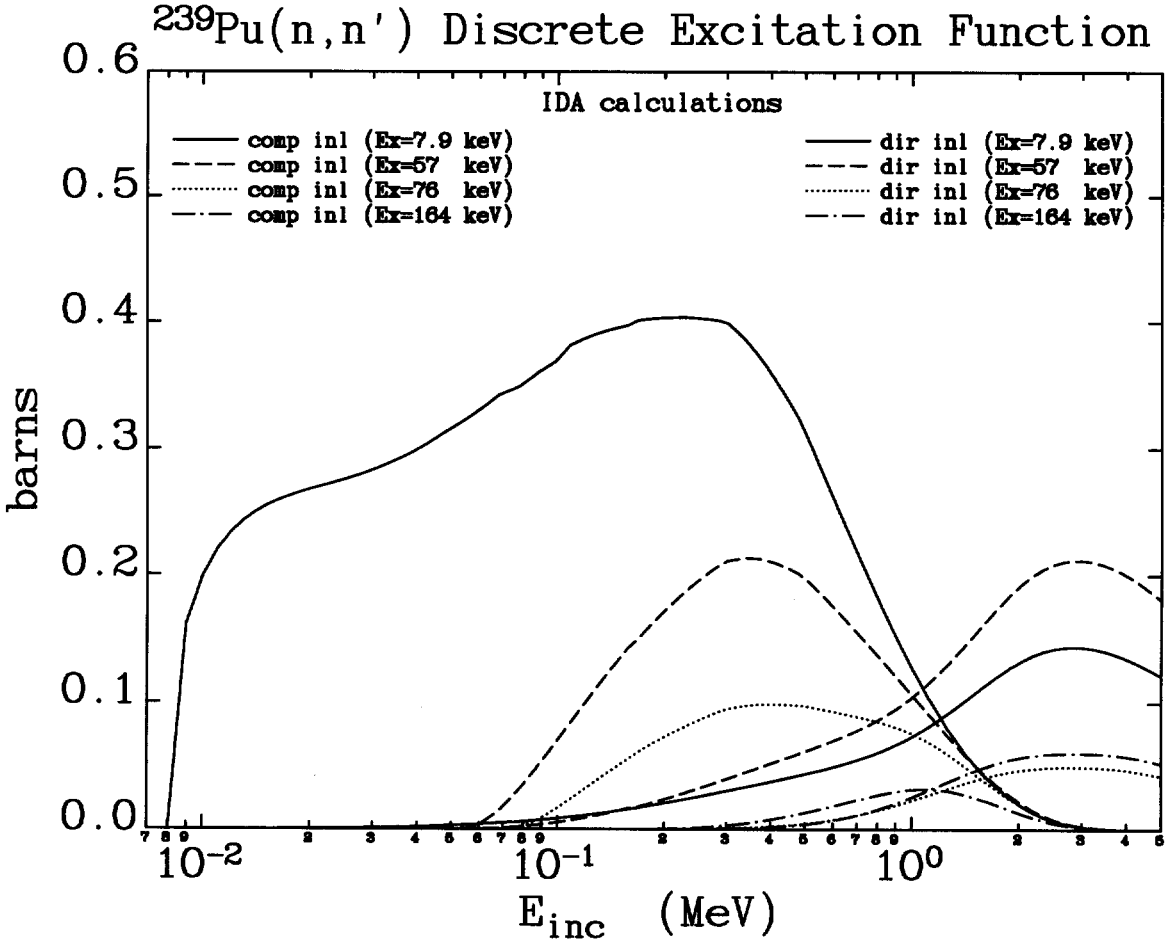

Figure 10: *The direct inelastic and compound inelastic scattering cross sections to the first four excited states of* ^{239}Pu *as a function of incident neutron energy.*

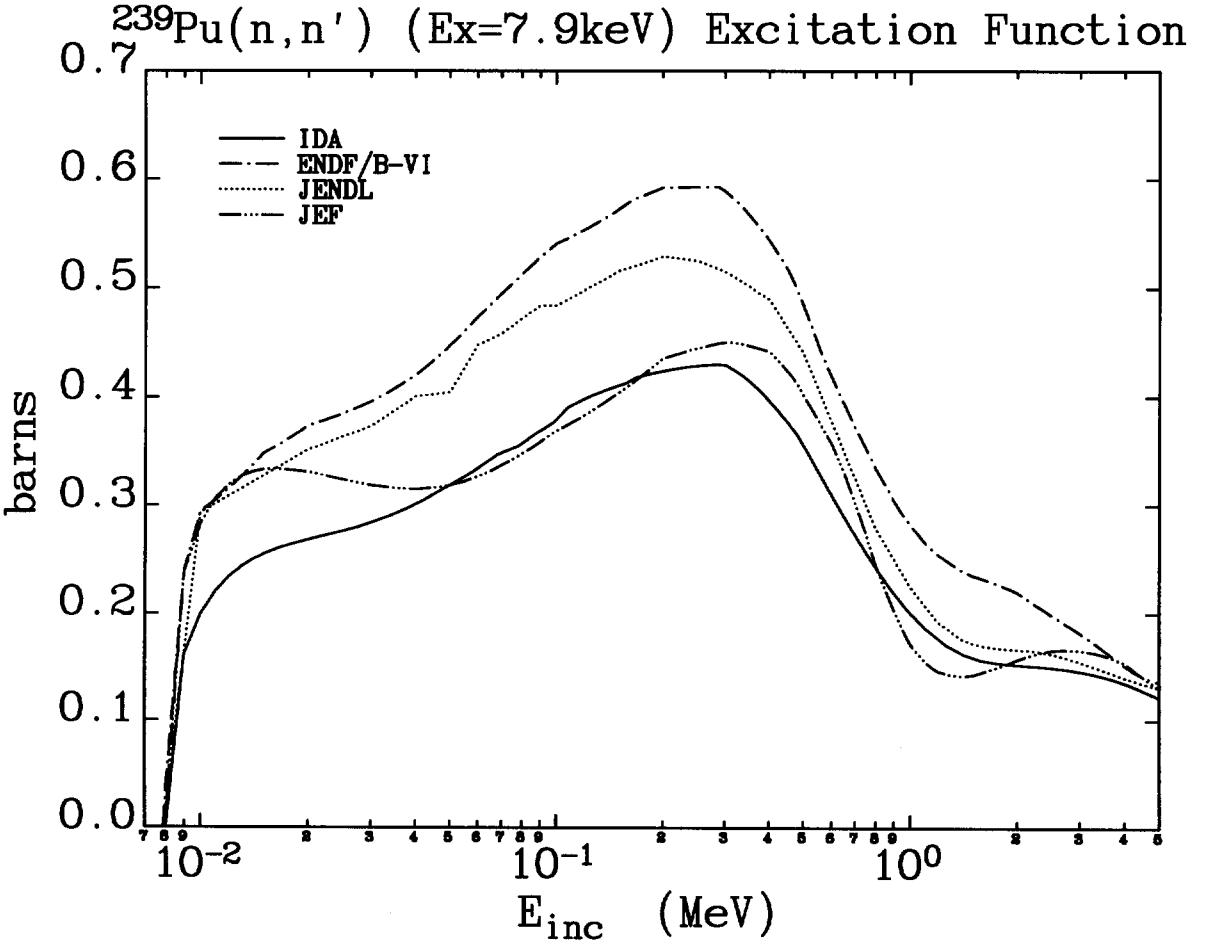

Figure 11: *The inelastic (direct + compound) scattering cross sections to the first excited state of ^{239}Pu as a function of incident neutron energy.*

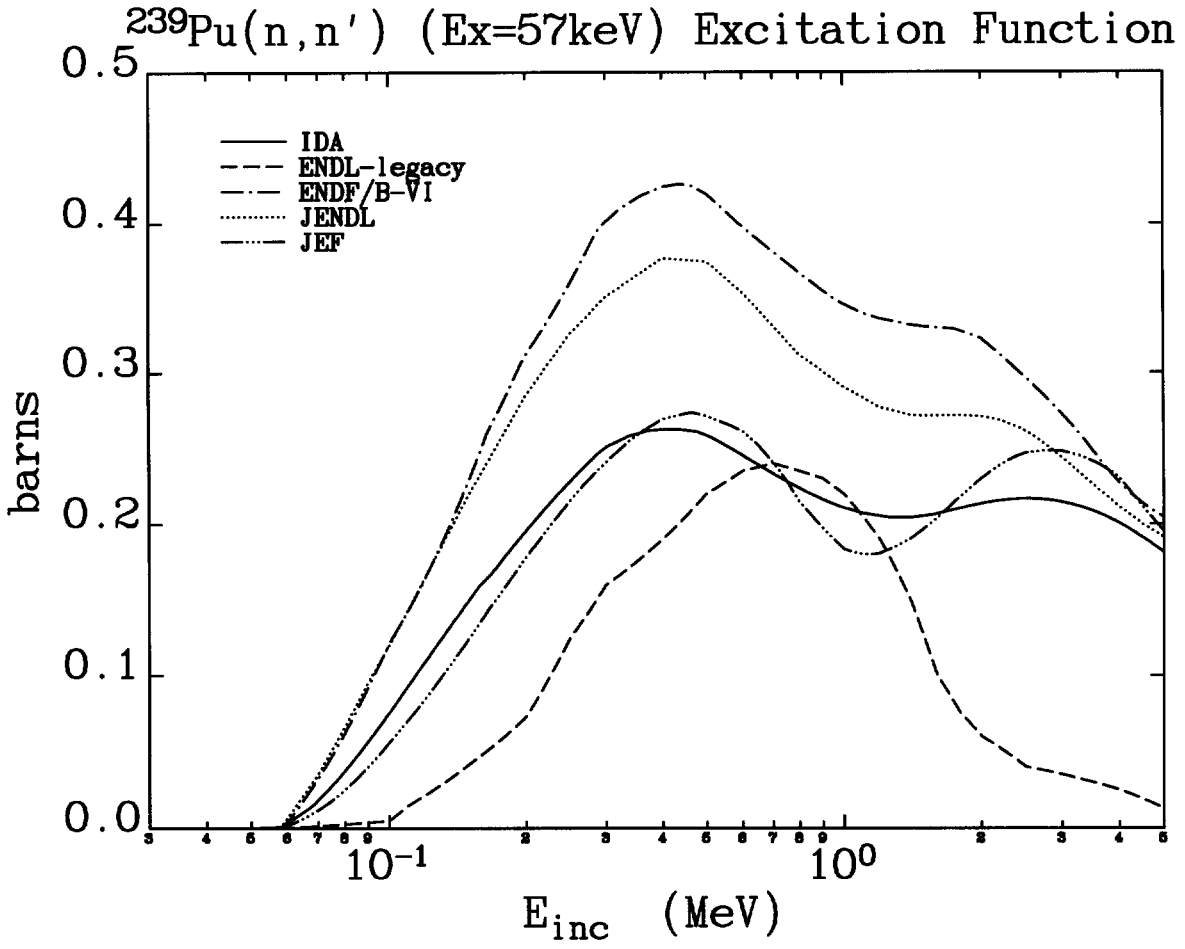

Figure 12: *The inelastic (direct + compound) scattering cross sections to the second excited state of ^{239}Pu as a function of incident neutron energy.*

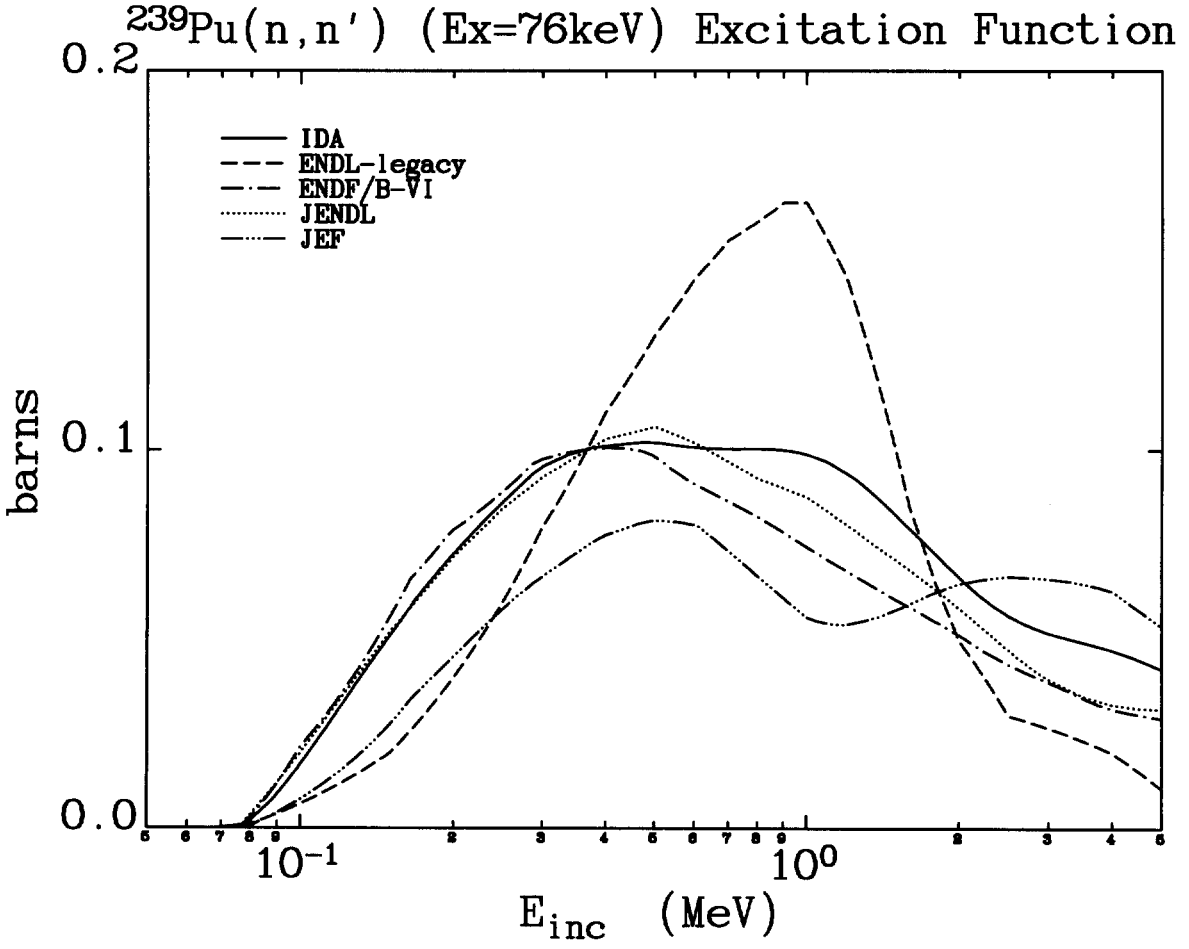

Figure 13: *The inelastic (direct + compound) scattering cross sections to the third excited state of ^{239}Pu as a function of incident neutron energy.*

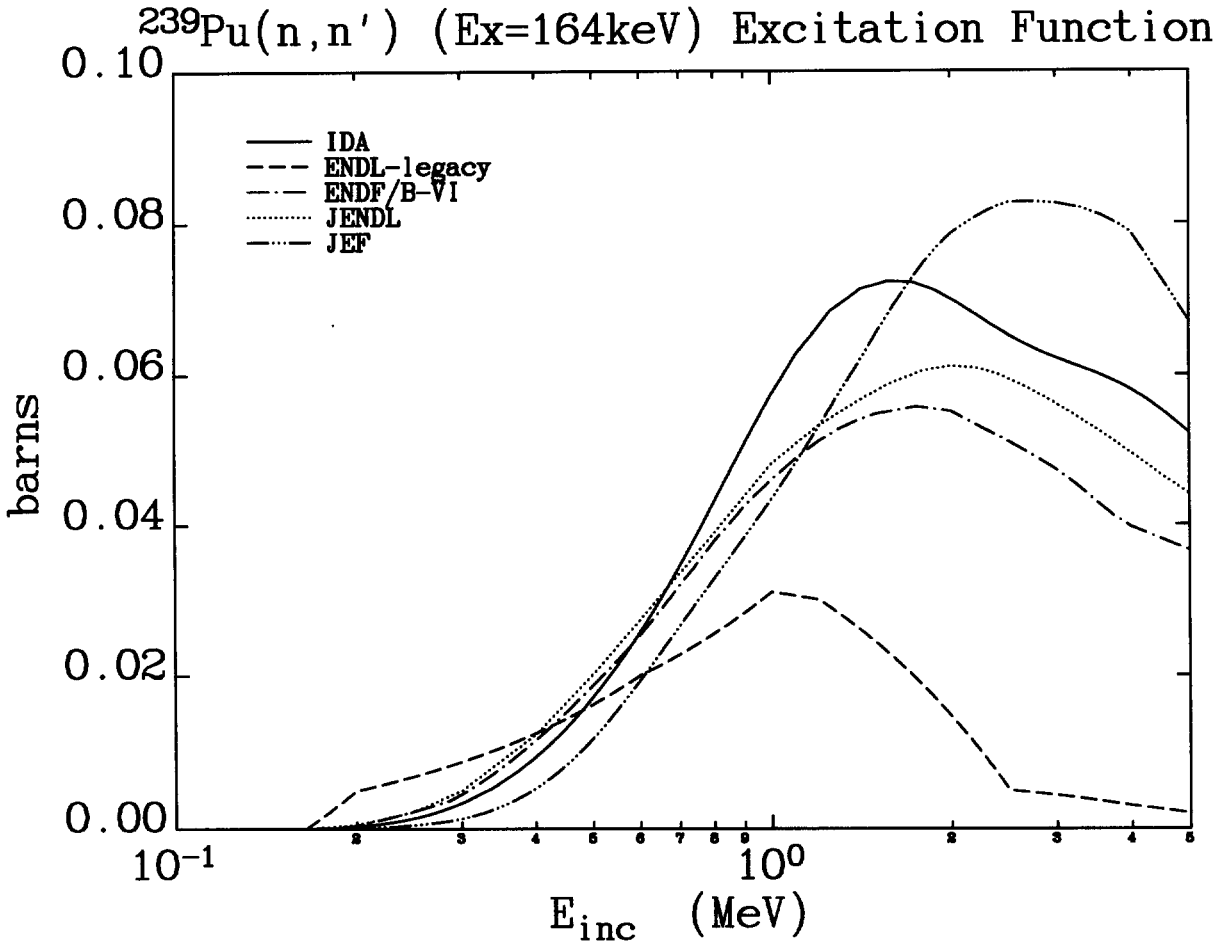

Figure 14: *The inelastic (direct + compound) scattering cross sections to the fourth excited state of* ^{239}Pu *as a function of incident neutron energy.*

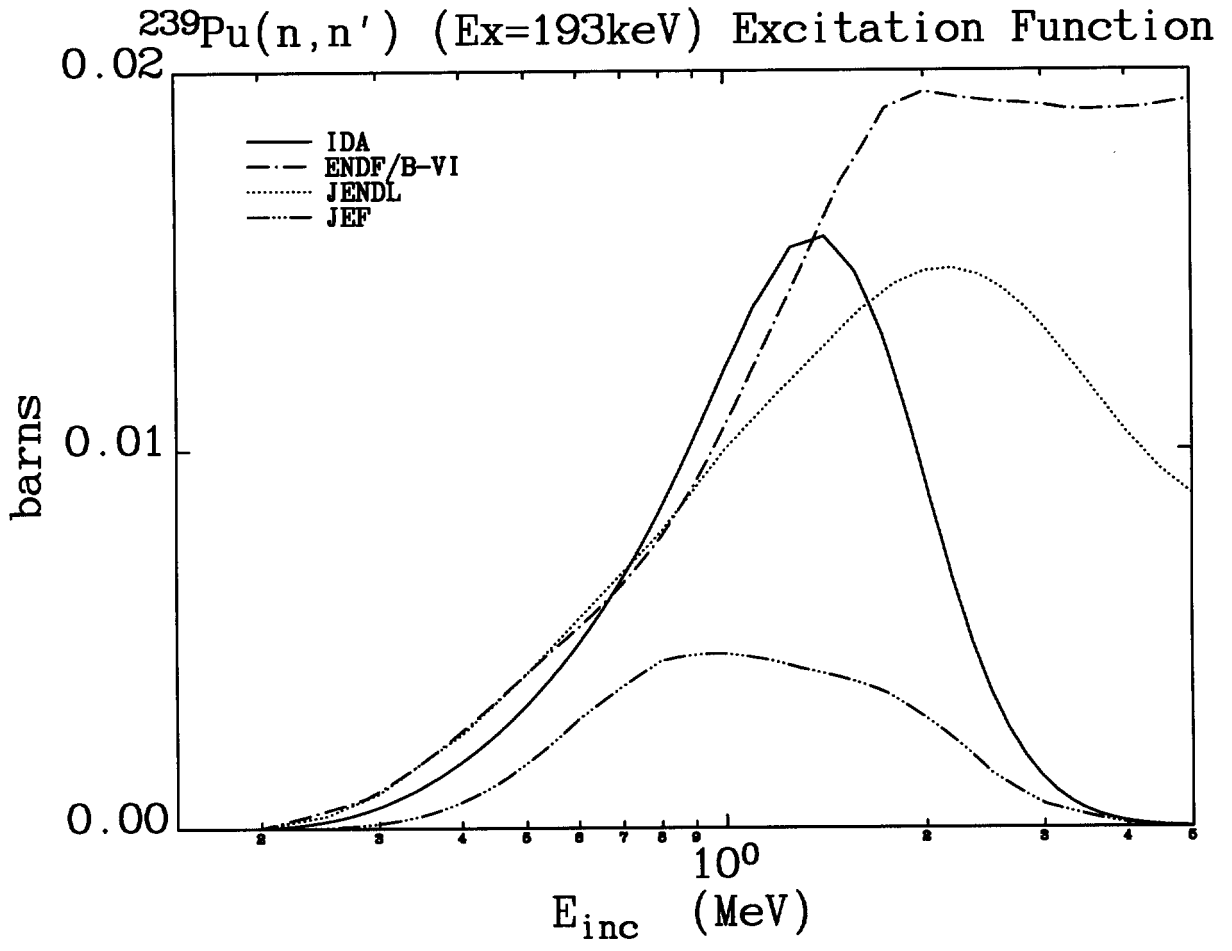

Figure 15: *The inelastic (compound only) scattering cross sections to the fifth excited state of* ^{239}Pu *as a function of incident neutron energy.*

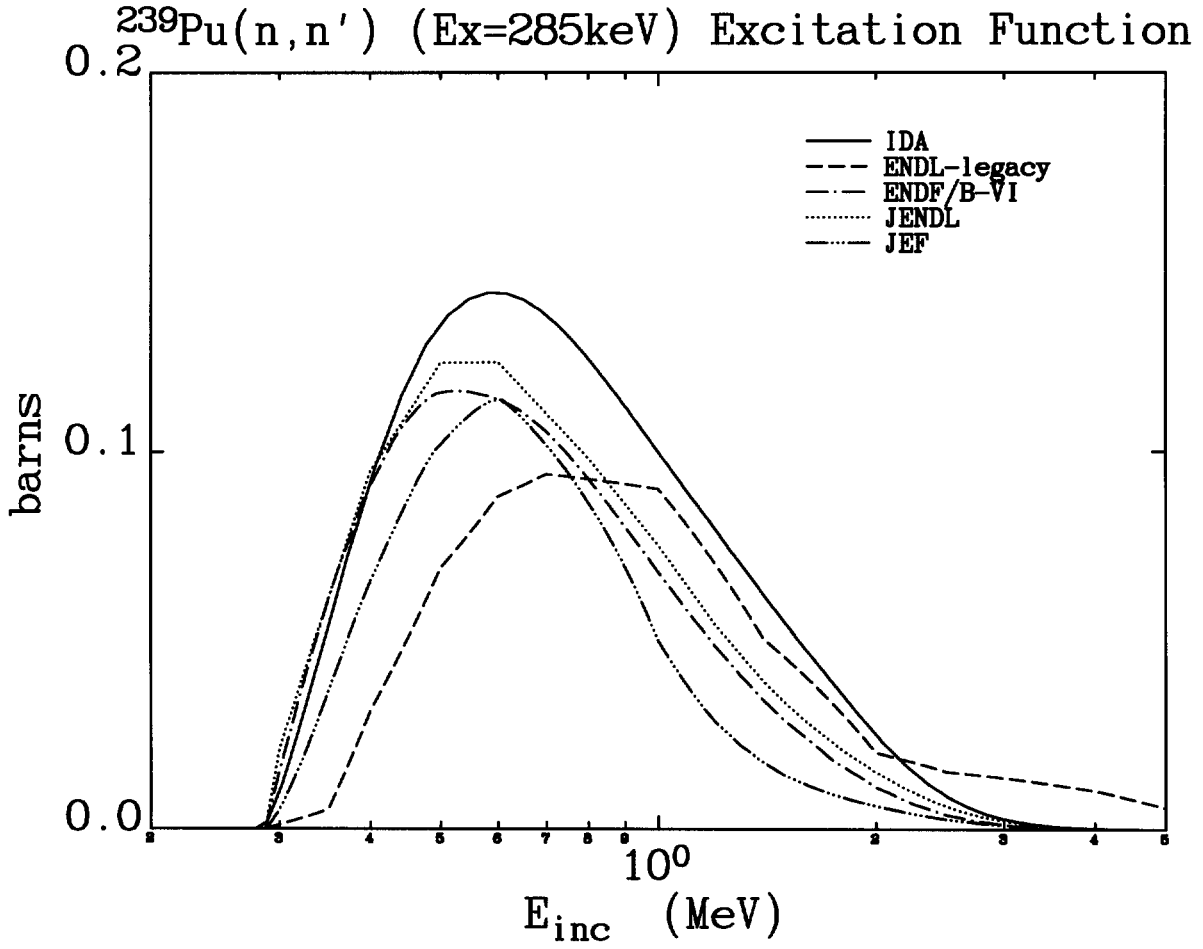

Figure 16: *The inelastic (compound only) scattering cross sections to the sixth excited state of* ^{239}Pu *as a function of incident neutron energy.*